Monthly Notices of the ROYAL ASTRONOMICAL SOCIETY

MNRAS **507,** 510–523 (2021) https://doi.org/10.1093/mnras/stab2184
Advance Access publication 2021 July 29

Stacked CMB lensing and ISW signals around superstructures in the DESI Legacy Survey

Qianjun Hang,★ Shadab Alam, Yan-Chuan Cai and John A. Peacock
Institute for Astronomy, University of Edinburgh, Royal Observatory, Blackford Hill, Edinburgh EH9 3HJ, UK

Accepted 2021 July 26. Received 2021 July 23; in original form 2021 May 25

ABSTRACT

The imprints of large-scale structures on the Cosmic Microwave Background (CMB) can be studied via the CMB lensing and Integrated Sachs–Wolfe (ISW) signals. In particular, the stacked ISW signal around supervoids has been claimed in several works to be anomalously high. In this study, we find cluster and void superstructures using four tomographic redshift bins with $0 < z < 0.8$ from the DESI Legacy Survey and measure the stacked CMB lensing and ISW signals around them. To compare our measurements with ΛCDM model predictions, we construct a mock catalogue with matched galaxy number density and bias and apply the same photo-z uncertainty as the data. The consistency between the mock and the data is verified via the stacked galaxy density profiles around the superstructures and their quantity. The corresponding lensing convergence and ISW maps are then constructed and compared. The stacked lensing signal agrees with data well except at the highest redshift bin in density peaks, where the mock prediction is significantly higher, by approximately a factor of 1.3. The stacked ISW signal is generally consistent with the mock prediction. We do not obtain a significant signal from voids, $A_{\rm ISW} = -0.10 \pm 0.69$, and the signal from clusters, $A_{\rm ISW} = 1.52 \pm 0.72$, is at best weakly detected. However, these results are strongly inconsistent with previous claims of ISW signals at many times the level of the ΛCDM prediction. We discuss the comparison of our results with past work in this area and investigate possible explanations for this discrepancy.

Key words: gravitational lensing: weak – cosmology: cosmic background radiation – cosmology: large-scale structure of Universe.

1 INTRODUCTION

The geodesics of photons in the Cosmic Microwave Background (CMB) are perturbed by their passage through intervening large-scale structures of the universe, generating effects from both spatial and temporal variations in the gravitational potential field, $\Phi(\mathbf{x}, t)$. Spatial gradients in Φ give rise to the gravitational lensing effect, which can be quantified by the lensing convergence κ:

$$\kappa(\hat{\mathbf{n}}) = \frac{1}{c^2}\int_0^{r_{\rm LS}} \frac{r_{\rm LS} - r}{r_{\rm LS} r}\nabla^2\Phi(\hat{\mathbf{n}}, r)\, dr, \tag{1}$$

where r is the comoving distance and $r_{\rm LS}$ is the comoving distance to the last scattering surface. This quantity effectively measures the total projected matter density between CMB and today weighted by a distance-dependent kernel for a given angular direction $\hat{\mathbf{n}}$. The temporal perturbation alters the temperature fluctuations of the CMB, leading to the Integrated Sachs–Wolfe (ISW) effect (Sachs & Wolfe 1967):

$$\frac{\Delta T(\hat{\mathbf{n}})}{T_{\rm CMB}} = -\frac{2}{c^2}\int_0^{t_{\rm LS}} \dot{\Phi}(\hat{\mathbf{n}}, t)\, dt, \tag{2}$$

where $T_{\rm CMB} = 2.725$K is the mean CMB temperature at redshift $z = 0$, and t in this expression denotes the look-back time. The ISW effect is intriguing because $\dot{\Phi} \neq 0$ in linear theory only in the era of late-time dark energy domination. The measurement of the ISW effect thus provides a dynamical probe for dark energy. The gravitational potential is related to the matter density fluctuation δ via the Poisson equation:

$$\nabla^2\Phi = \frac{3H_0^2\Omega_{\rm m}}{2a}\delta, \tag{3}$$

where δ is the fractional perturbation in the matter density and $a(t)$ is the dimensionless scale factor. In practice, the two imprints of potential fluctuations on the CMB can thus be studied using galaxy survey as tracers of the matter density field.

To measure the gravitational lensing and ISW signals, one approach is the angular cross-correlation between tomographic galaxy density fields and the CMB. The CMB lensing convergence map is reconstructed from the non-Gaussian features of the temperature fluctuations (Hu 2000; Okamoto & Hu 2003; Lewis & Challinor 2006). Given the galaxy selection function, the cross-correlation between the CMB lensing convergence and the large-scale structure can be detected at $>10\sigma$, both in spherical harmonic space and in angular space (e.g. Giannantonio et al. 2016; Singh, Mandelbaum & Brownstein 2017; Doux et al. 2018; Peacock & Bilicki 2018; Krolewski et al. 2020; Singh et al. 2020; Darwish et al. 2021; Hang et al. 2021). These measurements give constraints on the cosmological parameters $\Omega_{\rm m}$ and σ_8, as well as on the growth rate. Several of these works claim tensions in the $\Omega_{\rm m} - \sigma_8$ plane compared to the Planck constraints, and similar tensions are also present in

★ E-mail: qhang@roe.ac.uk

cosmic shear measurements (e.g. Joudaki et al. 2020; Asgari et al. 2021) at the $\sim 3\sigma$ level.

Similarly, ISW signals have been detected via cross-correlation (e.g. Fosalba, Gaztañaga & Castander 2003; Scranton et al. 2003; Cabré et al. 2006; Giannantonio et al. 2008; Ho et al. 2008; Stölzner et al. 2018; Hang et al. 2021), although the signal to noise is much lower for two main reasons. First, the signal is overwhelmed by the primordial temperature fluctuations in the CMB map, and secondly, the signal is concentrated at large scales (low multipoles), where the cosmic variance is largest owing to the small number of independent large-scale modes. One of the most significant detections made using tomographic cross-correlation is by Stölzner et al. (2018), who reached S/N $= 4.7\sigma$ by combining several galaxy surveys. The detection of this signal can be used to constrain the dark energy equation of state w, e.g. the analysis carried out in Stölzner et al. (2018).

Granett, Neyrinck & Szapudi (2008) took an alternative approach of pursuing a stacking analysis that was focused on superstructures. In this work, they averaged CMB temperature maps at the positions of 100 objects identified as voids and clusters that had the most extreme density contrasts as measured using the SDSS LRG sample. By comparison to ΛCDM simulations, they claimed an excess ISW signal of 4σ significance. Subsequently, Cai et al. (2014), Cai et al. (2017), Kovács et al. (2017), and Kovács (2018) used stacking techniques and claimed an ISW signal that was higher than the ΛCDM prediction at moderate significance. Nadathur & Crittenden (2016) reported a signal consistent with ΛCDM using the whole void catalogue, rather than focusing on superstructures. Most recently, Kovács et al. (2019), hereafter K19, measured the stacked ISW signal using the DES supervoids with radius $R_v > 100\,h^{-1}$ Mpc, and found an amplitude relative to the ΛCDM prediction of $A_{\rm ISW} = 5.2 \pm 1.6$ in combination with BOSS. In a separate paper, Vielzeuf et al. (2021) measured the stacked CMB lensing convergence signal for the same objects and found no discrepancy with ΛCDM.

The anomalous ISW amplitude from supervoids is of interest in terms of modified gravity, where the screening mechanisms in some theories are less effective in empty regions (Clampitt, Cai & Li 2013). However, there has not been a satisfactory explanation for this excess signal. Cai et al. (2014) argued that the signal is unlikely to be caused by Sunyaev-Zel'dovich effects, non-Gaussianity, or modified gravity (see also Nadathur, Hotchkiss & Sarkar 2012). Another possible explanation comes from the AvERA (Average Expansion Rate Approximation) model (Beck et al. 2018), which assumes an inhomogeneous expansion rate with $\Omega_\Lambda = 0$ and predicts a higher overall ISW signal by modifying the growth rate. However, Hang et al. (2021) showed that the AvERA model prediction is inconsistent with galaxy–temperature cross-correlation results, so the ability of the AvERA model to account for the supervoid results is subject to doubt.

One needs to be cautious in interpreting the stacked results. First, the definition of supervoids is not exactly the same in each case. In some cases, voids are defined in three-dimensional (3D) density fields based on e.g. the ZOBOV algorithm (Neyrinck 2008), whereas in other cases, the void definition is based on two-dimensional (2D) smoothed density fields (e.g. Sánchez et al. 2017). Different void-finding algorithms can lead to different structures being selected. Secondly, the procedures involve various parameter choices such as the initial smoothing scale of the density field and threshold criteria for superstructure selection. If an enhanced ISW signal is to be accepted as a genuine physical effect, it should be robust with respect to these different selection criteria.

Nevertheless, the reported anomalous ISW amplitudes are usually at the 2–3σ level, so it remains possible that they are statistical flukes. To clarify the situation, it is useful to use a bigger sample of galaxies for the analysis to beat down the dominant noise from sample variance. The aim of this work is to repeat the stacking analysis using superstructures in the DESI Legacy Imaging Survey. The large sky coverage reduces the noise due to cosmic variance. We use the galaxy maps produced in Hang et al. (2021), hereafter H21, based on photometric redshifts; the cross-correlation of these maps with the CMB lensing convergence and ISW effect provides a baseline for the ISW amplitude coming from superstructures only. We attempt to adopt the same void finding algorithm as in K19 based on the 2D maps, although the relatively high thickness of the photometric redshift bins means that our selected superstructures are not exactly comparable to those of K19. In order to reduce confirmation bias, we also adopt a 'blind' strategy where we fix our analysis pipeline using mock data based on cosmological N-body simulations, before we run the pipeline on the actual data.

The paper is organized in the following structure. Section 2 introduces the data used for creating superstructures, the mock galaxy data set, and the generated lensing convergence and ISW maps. The void-finding procedure and covariance matrix are described in Section 3. We compare our superstructure catalogues from the real and mock data in Section 4 and present the stacking results in Section 5. Finally, we discuss the results and sum up in Section 6.

2 DATA SET AND SIMULATION

2.1 DESI Legacy Survey

We utilize the galaxy density maps in four tomographic bins between $0 < z < 0.8$ constructed in H21 using the DESI Legacy Imaging Survey. In this section, we briefly describe the procedure by which these maps were constructed.

The DESI Legacy Imaging Survey (Dey et al. 2019) consists of observations from three different projects: divided around Dec $= 33^\circ$ in J2000 coordinates, the Southern hemisphere is observed by the Dark Energy Camera Legacy Survey (DECaLS; Flaugher et al. 2015; The Dark Energy Survey Collaboration 2005), whereas the Northern hemisphere is covered by Mayall z-band Legacy Survey (MzLS; Dey et al. 2016) and the Beijing–Arizona Sky Survey (BASS; Williams et al. 2004). The survey covers an area of 17 739 deg^2. The data used in this paper come from the publicly available Data Release 8.[1]

Oobjects with morphology type labelled point spread function (PSF) were excluded from the galaxy selection, and extinction correction was applied to the three optical bands g, r, and z, as well as the WISE (Wright et al. 2010) flux W_1. The following magnitude cuts were also applied: $g < 24$, $r < 22$, and $W_1 < 19.5$, in order to achieve uniform depth over the survey area. Survey incompleteness was quantified using Bitmasks,[2] with bits = (0, 1, 5, 6, 7, 11, 12, 13) masked. The photometric redshifts were calibrated for selected galaxies using the following spectroscopic samples: GAMA (DR2; Liske et al. 2015), BOSS (DR12; Alam et al. 2015), eBOSS (DR16; Ahumada et al. 2020), VIPERS (DR2; Scodeggio et al. 2018), and DEEP2 (Newman et al. 2013). In addition, we also included COSMOS (Ilbert et al. 2009) and DESY1A1 redMaGiC (Cawthon et al. 2018) for their highly accurate photometric redshifts. The spectroscopic samples were matched with DECaLS objects based

[1] http://legacysurvey.org/dr8/
[2] http://legacysurvey.org/dr8/bitmasks

on their nearest neighbours. All samples except the DESY1A1 redMaGiC sample were binned in 3D grids of $g - r$, $r - z$, and $z - W_1$ with a pixel width of about 0.03. Pixels containing more than five objects from the calibration samples were assigned the mean redshift of these objects. The DES samples were then processed in the same way to fill out pixels not assigned with redshift. This 3D grid was used to assign redshifts to 78.6 per cent of the selected Legacy Survey galaxies. The photometric redshifts of the catalogue were compared with that in Zhou et al. (2020), who applied a random forest method to assign photometric redshifts with a similar set of spectroscopic calibration samples. To improve the accuracy of photometric redshift, we further selected galaxies that have a difference of $|\Delta z| < 0.05$ between the two photometric redshifts. This removed a further 23.4 per cent of the sample.

These galaxies are separated into four tomographic bins: bin 0: $0 < z \leq 0.3$; bin 1: $0.3 < z \leq 0.45$; bin 2: $0.45 < z \leq 0.6$; and bin 3: $0.6 < z \leq 0.8$. We use `healpix` maps (Górski et al. 2005) with $n_{\rm side} = 512$ to construct galaxy density maps. The galaxy density is given by $\delta_{\rm g} = n/\bar{n} - 1$, where n is the number of galaxies in each pixel, and $\bar{n}$ is the mean number of galaxies.

The photometric redshift scatter in each tomographic bin is modelled by a modified Lorentzian of the form

$$L(x) = \frac{N}{(1 + ((x - x_0)/\sigma)^2/2a)^a}, \tag{4}$$

where N is a normalization such that $\int L(x)\,dx = 1$; x_0 is a shift in the mean redshift; σ controls the width of the scatter; and a controls the tail of the scatter. This function is convolved with the raw redshift distribution in order to model the underlying true selection function. Equation (4) provides a good fit to the calibration sample. To account for fainter galaxies, we allow x_0 and a to be free parameters and further impose that the sum of x_0 in four redshift bins to be zero. This results in seven nuisance parameters. In H21, we determined these parameters simultaneously with galaxy bias by fitting the 10 galaxy auto- and cross-correlations in spherical harmonic space between the four tomographic bins. We use the best-fitting photo-z parameters in this paper, with linear galaxy bias fixed at the minimum χ^2 value. The bias values in the four redshift slices are 1.25, 1.56, 1.53, and 1.83, respectively, assuming a fiducial *Planck* 2018 cosmology (Planck Collaboration VI 2018b).

There are two main systematic corrections applied to the galaxy density maps. The first one is survey completeness. Pixels with completeness <0.86 are masked, and the unmasked pixels are weighted by the inverse of the completeness. Using the ALLWISE total density map as a proxy for stellar density, we also correct systematics near the galactic plane. We introduce a cut in stellar density $N_{\rm star} < 1.29 \times 10^4\,{\rm deg}^{-2}$ and correct for the residual trend of $\delta_{\rm g}$ with $\log_{10}(N_{\rm star})$ by a fifth-order polynomial in each tomographic slice. We check the cross-correlations between the corrected density maps and the completeness map, as well as the ALLWISE total density map, and confirm that these are consistent with zero.

2.2 Simulation

We make use of the MultiDark Planck (MDPL2; Klypin et al. 2016) simulations with *Planck* 2013 cosmology. The simulation is performed with a $1\,h^{-1}$Gpc box with 3840^3 particles using the L-Gadget 2 codes. The mass resolution of the simulation is $1.51 \times 10^9\,h^{-1}\,M_\odot$. The simulation assumes a flat ΛCDM cosmology with $\Omega_{\rm m} = 0.307$, $\Omega_{\rm b} = 0.048$, $h = 0.67$, $n_{\rm s} = 0.96$, and $\sigma_8 = 0.823$. The dark matter halo catalogue for 32 snapshots between redshift 0 and 1 is processed using the ROCKSTAR[3] phase space halo finder (Behroozi, Wechsler & Wu 2013), in order to construct galaxy light-cones. The simulation is publicly available through the CosmoSim data base[4] (Prada et al. 2012; Riebe et al. 2013). Below, we describe the procedure used to generate various simulated DESI surveys.[5]

2.3 Simulated galaxy light-cones

We use the halo occupation distribution (HOD) model to generate simulated galaxy catalogues. We use only the measurements of linear and non-linear bias (H21) to find the best-fitting HOD parameters. We use a simplified version of the HOD model with only two free parameters corresponding to the characteristic mass of central ($M_{\rm cut}$) and satellite galaxies (M_1) as given in following equations:

$$p_{\rm cen} = \frac{1}{2}{\rm erfc}\left(\frac{\ln M_{\rm cut} - \ln M_{\rm halo}}{\sqrt{2}}\right) \tag{5}$$

$$\langle N_{\rm sat}\rangle = \frac{M_{\rm halo} - M_{\rm cut}}{M_1}, \tag{6}$$

where $p_{\rm cen}$ gives the probability of assigning a central galaxy to a halo with mass $M_{\rm halo}$ and $<N_{\rm sat}>$ gives the mean number of satellite galaxies as the function of halo mass. The actual number of satellite galaxies for any given halo is drawn from a Poisson distribution. We use main haloes (i.e. discarding subhaloes) from 32 snapshots between redshifts 0 and 1 and determine the best-fitting HOD parameters by fitting the 3D galaxy power spectrum with linear and non-linear bias evolution as measured in the data (H21). The linear bias values in our mocks are defined using scales $0.05 < k < 0.1\,h\,{\rm Mpc}^{-1}$ and the non-linear bias uses the scales $0.5 < k < 2\,h\,{\rm Mpc}^{-1}$. Our best-fitting parameters are not very sensitive to the limits of scales used to define the linear and non-linear bias. The best-fitting HOD parameters along with galaxy bias are shown in the Fig. 1. We have created two sets of mocks, one of which matches only the linear bias, and the other one also has non-linear bias matched. For the scales considered in this project, we confirm that the two mocks do not give rise to significantly different stacking signals from superstructures.

We then convert our galaxy catalogue into light-cone form by simply repeating the box and placing the observer at the origin in order to extract shells from each snapshot covering the comoving separation between consecutive snapshots. The simulation and data are matched in galaxy number density in each redshift slice. In order to include the photometric redshift effect, we assign to each galaxy a photometric redshift $z_p = z + \delta z$, where δz is drawn from the distribution of equation (4) with the parameters given by the best fit $p(z)$ in each bin from H21. We then construct our tomographic slices by selecting galaxies in redshift bins using z_p. The resulting true redshift distribution is close to the best fit $p(z)$ from the real data, as shown in Fig. 2. The same survey mask is applied to the mock as the DESI Legacy Survey data.

2.4 Making mock lensing convergence maps

In order to generate lensing convergence maps that are consistent with our simulated galaxy data, we perform the following integral

[3] https://bitbucket.org/gfcstanford/rockstar
[4] https://www.cosmosim.org/cms/simulations/mdpl2/
[5] These products are publicly available at https://gitlab.com/qianjunhang/desi-legacy-survey-superstructure-stacking

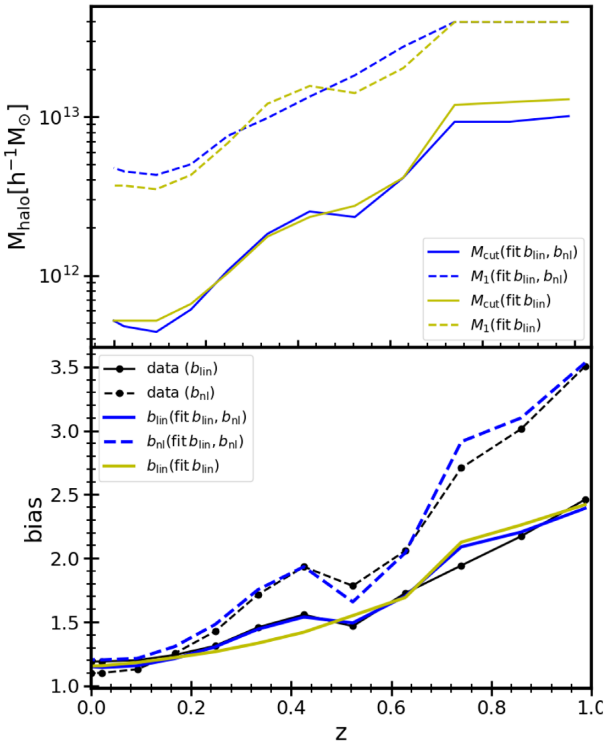

Figure 1. Top panel shows the best-fitting HOD parameters as the function of redshift used to generate simulated galaxy catalogues. Bottom panel shows the evolution of linear and non-linear bias in mock with coloured lines. The black line shows the best-fitting linear and non-linear bias obtained for the data from Hang et al. (2021).

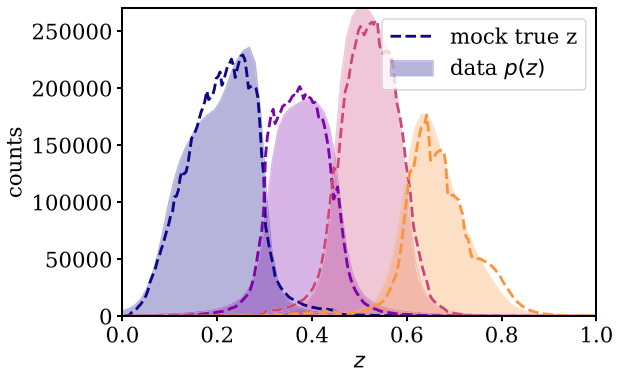

Figure 2. The mock redshift distribution (dashed) is matched to observations by assigning a redshift error δz from the best-fitting modified Lorentzian distribution used in Hang et al. (2021) and the corresponding best fit $p(z)$ from data (shaded) by fitting the galaxy auto- and cross-correlations in the four tomographic bins.

using the Born approximation:

$$\kappa(\hat{\theta}) = \int_0^{r_{\rm max}} \frac{3H_0^2\Omega_{\rm m}}{2c^2}\frac{(r_{\rm LS}-r)r}{r_{\rm LS}}\delta(r,\hat{\theta})\,dr, \tag{7}$$

where $r_{\rm LS}$ is the comoving distance between CMB and the lens plane and r is the comoving distance to the lens plane. The $\delta(r,\hat{\theta})$ is the matter overdensity in the direction $\hat{\theta}$ within a shell of width dr at distance r. To determine δ, we first create particle light-cone using snapshot by repeating the box and extracting a shell of particle at the location of 32 halo snapshot between redshifts 0–1. But we have only three particle snapshots ($z \approx 0$, 0.49, and 1.02) available compared to 32 halo snapshot. Therefore, for each halo snapshot shell, we use the nearest particle snapshot and scale the overdensity by ratio of growth at the halo snapshot to the growth at nearest particle snapshot. This gives us $\delta(r,\hat{\theta})$, which is then integrated using equation (7). In principle, the full κ map should be integrated with $r_{\rm max} = \infty$. But since we are concerned with only the cross-correlation of galaxies with the convergence map, as long as we limit our integral to larger than the maximum galaxy redshift ($z \approx 0.9$), we will obtain unbiased results. Therefore, we use $r_{\rm max}$ corresponding to $z_{\rm max} = 1.02$ to generate our lensing convergence map. We note that we use a `healpix` pixelization with $n_{\rm side} = 512$ to generate our convergence map.

2.5 Making ISW maps in simulations

Although the ISW signal arises from the linear evolution of the potential Φ, it has contributions from non-linear evolution. To include both of them, we follow the algorithm presented in Cai et al. (2010) and Seljak (1996) to compute the time derivative of the potential $\dot{\Phi}$ in Fourier space using

$$\dot{\Phi}(\vec{k},t) = \frac{3}{2}\left(\frac{H_0}{k}\right)^2\Omega_{\rm m}\left[\frac{\dot{a}}{a^2}\delta(\vec{k},t) + \frac{i\vec{k}\cdot\vec{p}(\vec{k},t)}{a}\right], \tag{8}$$

where a is the expansion factor at z, $\vec{p}(\vec{k},t)$ is the Fourier transform of the momentum density fluctuation $\vec{p}(\vec{x},t) = [1+\delta(\vec{x},t)]\vec{v}(\vec{x},t)$, and $\delta(\vec{k},t)$ is the density contrast. We use the full-particle data at the three snapshots mentioned above to compute $\dot{\Phi}(\vec{k},t)$ in Fourier space. We then interpolate $\dot{\Phi}$ in Fourier space according to the linear growth factor $G(a) = D(a)[1-f(a)]$ to obtain $\dot{\Phi}(\vec{k},t)$ at more epochs t between the original snapshots, where the times t are chosen such that their line-of-sight comoving spacing is $100\,h^{-1}$ Mpc. The inverse Fourier transform of the above yields $\dot{\Phi}$ in real space on 3D grids. Following Cai et al. (2010), we then use HEALPIX to tessellate the sky and follow HEALPIX pixel centres along the line of sights to interpolate and integrate $\dot{\Phi}$ values on grids to obtain the full ISW maps including the non-linear Rees-Sciama effect (Rees & Sciama 1968). Examples of the power spectra measured from these maps are shown in Fig. 3.

2.6 Quasi-linear ISW maps

With the expected high signal to noise from the galaxy–CMB lensing cross-correlation, we can also use the observed lensing signal around peaks and troughs to predict their corresponding ISW signal directly. This has the benefit of using one observable to predict the other. Using equation (7), we compute the lensing convergence κ for each direction $\hat{\theta}$ in each shell between $0 < z < 1$.

The κ map can then be converted to the lensing potential, ψ, via

$$\kappa_{\ell m} = \frac{1}{2}\ell(\ell+1)\psi_{\ell m}. \tag{9}$$

This is related to the 3D gravitational potential Φ via

$$\psi(\hat{\theta}) = -\frac{2}{c^2}\int\frac{r_{\rm LS}-r}{r_{\rm LS}r}\Phi(\hat{\theta},r')\,dr'. \tag{10}$$

The ISW signal is related to the derivative of the gravitational potential via equation (2). For the Poisson equation, $\nabla^2\Phi = (3/2)H_0^2\Omega_{\rm m}\delta/a$. In linear theory, it follows that $\nabla^2\dot{\Phi} = H(1-f)\nabla^2\Phi$, or $\dot{\Phi} = H(1-f)\Phi$. Note that $\dot{\Phi}$ calculated in this way is not fully linear, because the 3D potential includes contributions from non-linearity. The key assumption is that the density and velocity are linearly coupled.

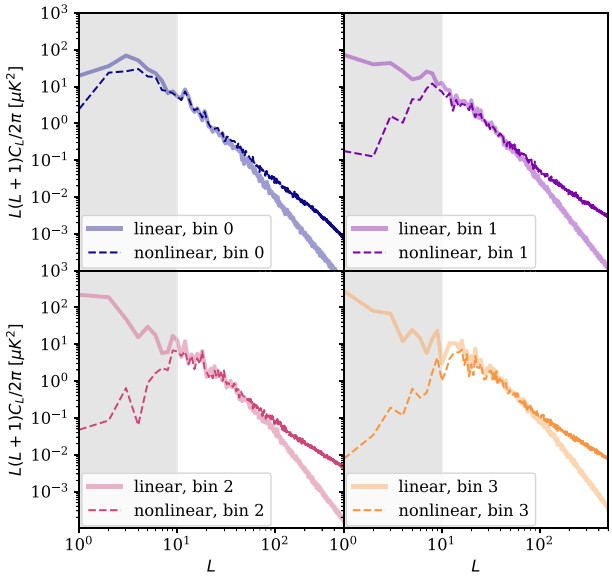

Figure 3. The auto power spectra of simulated ISW maps for the mock catalogue in four tomographic slices. The full non-linear computation is shown with dashed lines and the quasi-linear approximation is shown with solid lines. The grey region indicates the low-ℓ range that is removed in the linear map.

Given a thin shell centred around redshift z_0 with edges $[z_0 - \Delta z, z_0 + \Delta z]$, one can make the approximations

$$\psi(\hat{\theta}, z_0) \approx -\frac{2}{c^2}\frac{r_{\rm LS} - r_0}{r_{\rm LS} r_0}\frac{c}{H(z_0)}\int_{z_0-\Delta z}^{z_0+\Delta z}\Phi(\hat{\theta}, z)\,dz, \tag{11}$$

$$\Delta T(\hat{\theta}, z_0) \approx -T_0\frac{2}{c^2}a(z_0)[1 - f(z_0)]\int_{z_0-\Delta z}^{z_0+\Delta z}\Phi(\hat{\theta}, z)\,dz. \tag{12}$$

Combining these two equations, we have

$$\Delta T(\hat{\theta}, z_0) \approx T_0 a(z_0)[1 - f(z_0)]\frac{r_{\rm LS} r_0}{r_{\rm LS} - r_0}\frac{H(z_0)}{c}\psi(\hat{\theta}). \tag{13}$$

We obtain the ISW map for each of the 30 shells, where r_0 is the comoving distance to the shell centre. These maps are then added together to produce the final (noise-free) ISW map. The comparison of the power spectra of the quasi-linear and full ISW maps is shown in Fig. 3. We can see that the two maps are most consistent in the range of $10 < \ell < 40$. At scales $\ell \lesssim 10$, the linear map gives unphysical modes whose amplitudes are much larger than the full computation. At smaller scales, where $\ell > 40$, the full computation gives a higher amplitude than the quasi-linear case. In the stacking analysis, we are mostly interested in structures of a few degrees corresponding to $\ell \sim 100$.

3 METHODS

3.1 Blind analysis

Given the low significance of the tentative ISW signal from stacking, we wish to conduct the calibration for the selection of superstructures strictly prior to the unveiling of the stacked temperature results, i.e. a blind analysis. For this, we separate our analysis into two steps: (1) we finalize our selection for superstructures based on the galaxy number density maps and their cross-correlations with the CMB lensing convergence map. The stacking with CMB lensing map is expected to yield much higher signal to noise; thus, it provides a benchmark for the calibration of our superstructures. (2) We then 'unblind' by applying the same stacking with the same catalogues of superstructures for the CMB temperature map.

3.2 Void finder

We follow the void finder algorithm in Sánchez et al. (2017). The finder takes the following steps:

(i) Given the 2D density fluctuation on `healpix` maps with $\delta = n/\bar{n} - 1$, we first apply a Gaussian smoothing of $\sigma = 20\,h^{-1}\,{\rm Mpc}/d(z)$, where $d(z)$ is the mean comoving distance to the tomographic slice. We then define pixels with $\delta < \delta_*$ as potential void centres. In practice, we fix δ_* to pick out the lowest 10 per cent of the smoothed pixels, which is around $\delta_* = -0.2$.

(ii) Starting from the lowest density pixel in the potential void centres, we compute the mean density δ_i inside circular shells of radii R_i and $R_i + \Delta R$ for each $R_i \in \{R\}$. ΔR is chosen to be $1\,h^{-1}$ Mpc. Once $\bar{\delta}_i > 0$ is encountered for the first time, we register $R_v = R_i + \Delta R/2$ as the void radius. In practice, we use the `healpy.query_disc` function to find pixels within a disc of angular size $\theta_i = R_i/d(z)$.

(iii) Once the void is found, we check the potential void centre list and exclude any centre that is inside the existing void.

(iv) We then update the list of potential void centres and repeat steps (ii)–(iii) until the list is exhausted.

The free parameters in this finder algorithm are the initial smoothing σ and the density cut δ_*. A larger σ will result in the merging of smaller voids and could lead to higher signal to noise (Sánchez et al. 2017; Kovács et al. 2019). As a result of merging voids and the hierarchical void-finding procedure, the void catalogue can be different. Increasing δ_* would include shallower voids. However, this should not affect any deeper voids found with a lower δ_*. It is possible to find small but deep voids embedded in large shallower voids. We choose $\{R\}$ in the range $1\,h^{-1}\,{\rm Mpc} \le R \le 300\,h^{-1}\,{\rm Mpc}$, with an increment of $2\,h^{-1}$ Mpc between each step. After we obtain the void sample, we further exclude voids that have less than 70 per cent of their area inside the survey mask. An illustration of the procedure is shown in Fig. 4.

A major difference between this work and Kovács et al. (2019) is that our redshift slice is much thicker whereas they used slices of comoving size $100\,h^{-1}$ Mpc. In Kovács et al. (2019), due to the thin redshift slice, they also pruned overlapping voids between different redshift bins by shifting the bin edges a few times. Thus, although the void-finding algorithm is defined in 2D, their void catalogue is comparable to those found using 3D algorithms. We do not carry out this procedure here because we expect that the structures in the four tomographic bins are dominated at distinctive redshifts and thus not strongly correlated. The voids found here are likely to be 'tunnels' rather than spherical objects.

To find clusters, we apply an identical procedure to an inverted density map. Due to the lognormal shape of the smoothed density distribution of each map, we select the densest 5 per cent, instead of 10 per cent, pixels as potential centres. This choice gives similar numbers of clusters and voids in the final sample.

In order to obtain the stacked signal at the position of these superstructures, we rotate the map (in this case, the map can be galaxy density, lensing convergence, or temperature fluctuation) at the pixel level to place each superstructure centre at $(\theta, \phi) = (0, 0)$. We then stack the rotated maps scaled by the void radius R_v, on a grid with $0 \le R \le 3R_v$. To account for masks, we also perform the same rotation to the mask for each void. The stacked map is obtained

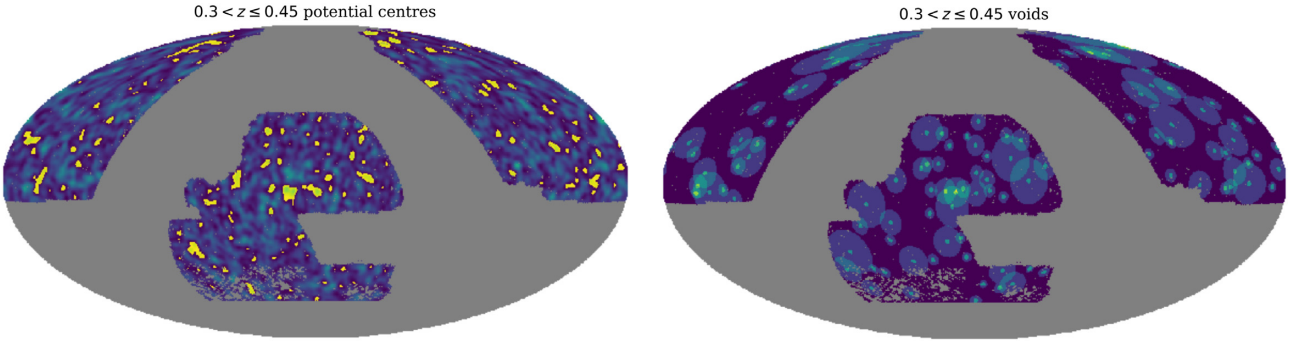

Figure 4. An example of the void-finding procedure using the tomographic slice in redshift range $0.3 < z \leq 0.45$. Left: the highlighted pixels correspond to the potential void centres, selected on the smoothed density map with $\delta < \delta_*$. In this case, $\delta_* = -0.14$. The background intensity map shows the density fluctuation in this slice. Right: The resulting void centres (shown highlighted dots) and their void radius (shown in fainter circles). Notice that some voids at survey boundaries are excluded. Also notice that voids can overlap, in cases where deeper voids can be found inside shallower voids.

by

$$P^{\rm stack} = \frac{\sum_i P_i^{\rm map}}{\sum_i P_i^{\rm mask}}, \tag{14}$$

where $P_i^{\rm map}$ is the pixel value for the map for i-th void, and $P_i^{\rm mask}$ is that for the mask. We extract the isotropic radial profile for these stacked images. Given the angular bins $\{\theta\}$, we measure the average signal in the ring between radii θ_i and θ_{i+1} and assign the value to the middle of the angular bin.

3.3 Covariance matrix

We use three methods to estimate the covariance matrix for the stacked signal to account for the noise on the background CMB map as well as the foreground superstructure positions.

To capture the CMB noise, we generate 1000 random CMB maps with $n_{\rm side} = 512$ using the measured pseudo CMB temperature auto power spectrum, corrected by the fraction of sky lost due to the mask $\hat{C}_\ell = C_\ell / f_{\rm sky}$. The maps are then generated using the `synfast` function in the `healpy` package applied to C_ℓ and multiplied by the *Planck* 2018 CMB mask. For comparison, we also use the *Planck* best-fitting ΛCDM CMB power spectrum,[6] accounting for the pixel window function and the FWHM = 5 arcmin circular Gaussian smoothing. These methods give a consistent covariance matrix. We repeat the same stacking process for superstructures in each redshift slice on each of the random CMB maps and extract the averaged radial profile. The covariance matrix is computed by

$$C_{ij} = \frac{1}{N} \sum_s^N \left(x_i^s - \bar{x}_i\right)\left(x_j^s - \bar{x}_j\right), \tag{15}$$

where $N = 1000$ is the sample size, x_i^s is the measurement of i-th data component in the s-th sample, and $\bar{x}_i$ is the mean measurement of the i-th component. The inverse covariance is corrected by the Hartlap factor (Hartlap, Simon & Schneider 2007) with $C_{ij}^{-1} = (N - p - 1)/(N - 1)\langle C_{ij}^{-1}\rangle$, where $p = 15$ is the length of the data vector.

To estimate the errors due to the fluctuations of the foreground galaxy sample, we generate 1000 sets of random void (cluster) positions for each redshift bin within the survey mask and compute the stacked signal on the *Planck* 2018 CMB temperature map (Planck Collaboration I 2018a). It should be noticed that this assumes no correlation of the positions of the voids (clusters), which is in general not true: there will be close pairs of clusters, while it is unlikely to find two voids that are close to each other. Nevertheless, this method provides a rough estimate of the foreground random error. The covariance is computed using equation (15) and the inverse covariance is corrected by the Hartlap factor.

Finally, we estimate the covariance matrix from Jackknife subsampling by excluding one void (cluster) at a time in the given redshift bin. The sample size is equal to the number of voids (clusters) in each bin, N_J. The resultant covariance matrix from equation (15) is multiplied by $(N_J - 1)$ to account for the correlation between different Jackknife samples. The Jackknife covariance matrix is noisy with small sample size, i.e. in the lower redshift bins.

The comparison of the diagonal elements of the three covariance matrices for the void sample is shown in Fig. 5. For the cluster sample, the covariance is similar but with different number of objects in each bin. In all cases, there is close agreement between the three methods. Due to the small Jackknife sample size in bin 0, the diagonal elements are noisy compared to the other two methods. From here on, we will use the covariance matrix estimated from random superstructure positions in our following analysis. The Jackknife covariance is used for the case of the stacking of all superstructures.

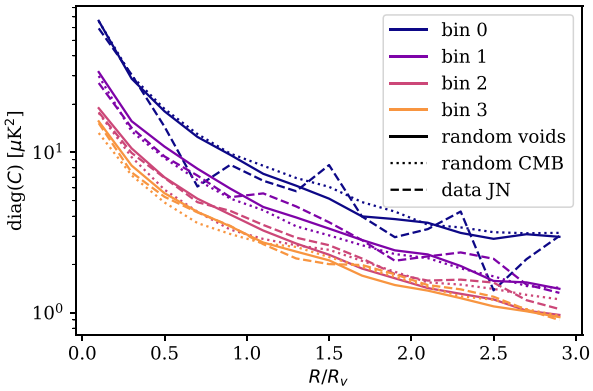

Figure 5. The diagonal elements of the covariance matrices (in $[\mu K^2]$) for the radial ISW stacked profile in each redshift bin (shown in different colours). The dotted lines show that from 1000 random CMB samples using the void positions in data, the solid lines show that from 1000 sets of void positions using the real CMB map, and the dashed lines show the Jackknife error from the actual data.

[6] http://pla.esac.esa.int/pla/#cosmology

Table 1. Summary of various parameters used in superstructure finding and the number of superstructures in each redshift slice for the mock and data, respectively. The first two rows show the mean redshift computed from the best-fitting redshift distribution and the linear galaxy bias in H21. The third row shows the smoothing scales for the density maps in units of degrees, which correspond to a comoving length of $20\,h^{-1}$ Mpc for each slice. The last few rows show the density cut, where $\delta < \delta_*$ ($\delta > \delta_*$) are selected as potential void (cluster) centres, as well as the number of objects found in each bin, after excluding those that have less than 70% of their area inside the survey mask.

Redshift bin	$0 < z \leq 0.3$	$0.3 < z \leq 0.45$	$0.45 < z \leq 0.6$	$0.6 < z \leq 0.8$
Mock				
Mean redshift	0.210	0.376	0.521	0.667
Linear bias	1.19	1.40	1.49	1.76
Smoothing scale (deg)	1.92	1.12	0.84	0.68
δ_* (voids)	−0.11	−0.14	−0.14	−0.15
N (voids)	28	108	209	364
δ_* (clusters)	0.11	0.15	0.15	0.16
N (clusters)	31	119	230	378
Data				
Mean redshift	0.207	0.376	0.522	0.663
Linear bias	1.25	1.56	1.52	1.83
Smoothing scale (deg)	1.93	1.09	0.84	0.69
δ_* (voids)	−0.11	−0.14	−0.14	−0.15
N (voids)	33	111	223	332
δ_* (clusters)	0.12	0.16	0.16	0.18
N (clusters)	38	97	185	282

4 SUPERSTRUCTURES

A summary of the numbers of voids and clusters found in each redshift bin is shown in Table 1 for both the mock and the real data. In general, the data and the mock show good consistency in terms of the number of voids found and in the distribution of void radius. For clusters, the density cut δ_* in the finder algorithm is slightly larger in data compared to mock, and the number of clusters found is smaller especially in bin 2 and bin 3. The distribution of the radius in comoving length and central density (in the smoothed map) of these superstructures is shown in Fig. 6. The majority of the superstructures found have a radius of around $60\,h^{-1}$ Mpc, with an extended tail towards $R_v \sim 300\,h^{-1}$ Mpc. There is a small number of clusters in data that saturate at the maximum radius. It is pointed out in Kovács et al. (2017) that there is an anticorrelation between the depth and the size of the superstructures. There is, however, no clear trend in the voids and clusters found here. The minimum R_v at fixed central density increases with the central density becoming more extreme.

The stacked galaxy density profiles are shown in the upper panel of Fig. 7 for both voids and clusters. The agreement between mock (solid bands) and real data (circles for voids and squares for clusters) is good. The dotted lines show the profile divided by linear galaxy bias in each case. The agreement between data and simulation using linear bias is expected for voids, as discussed in Pollina et al. (2017). At $R > R_v$, the stacked density profile changes sign and peaks at $R \sim 1.3R_v$, before falling to zero at larger scales. This suggests that on average, the voids found are surrounded by overdensities and clusters are surrounded by underdensities.

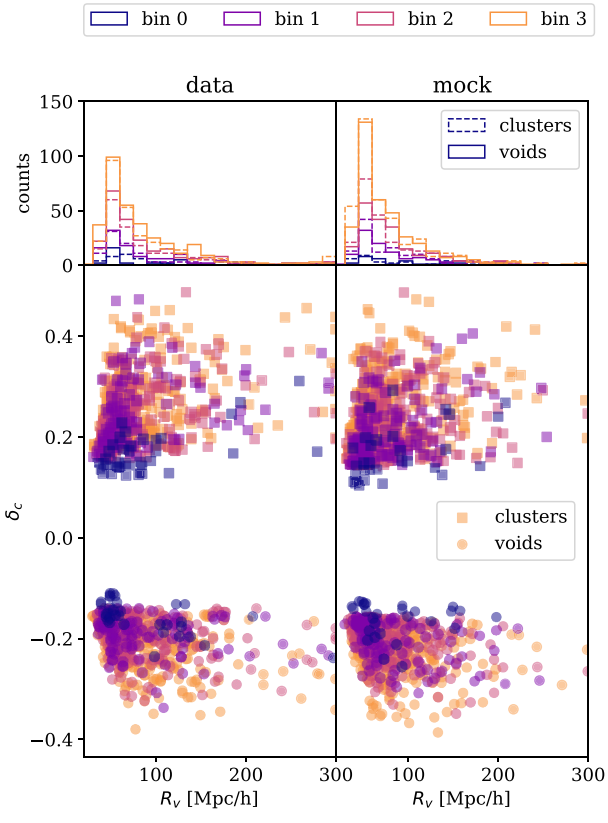

Figure 6. Superstructure size (R_v) and central density (δ_c) in data and the mock for each redshift bin. The radius is defined as when the mean density measured within a ring of central radius R and width $1\,h^{-1}$ Mpc first become positive.

5 RESULTS

5.1 Stacked lensing map

We stack the *Planck* 2018 lensing convergence map (Planck Collaboration VIII 2018c) with $\ell_{\rm max} = 2048$ and the simulated lensing convergence map at superstructure positions in real and mock data, respectively. Prior to stacking, we smoothed the lensing maps with a Gaussian kernel with full width at half-maximum (FWHM) = 1° to suppress the small-scale power for the purpose of map rotation at the pixel level, and this is done consistently in both data and simulation.

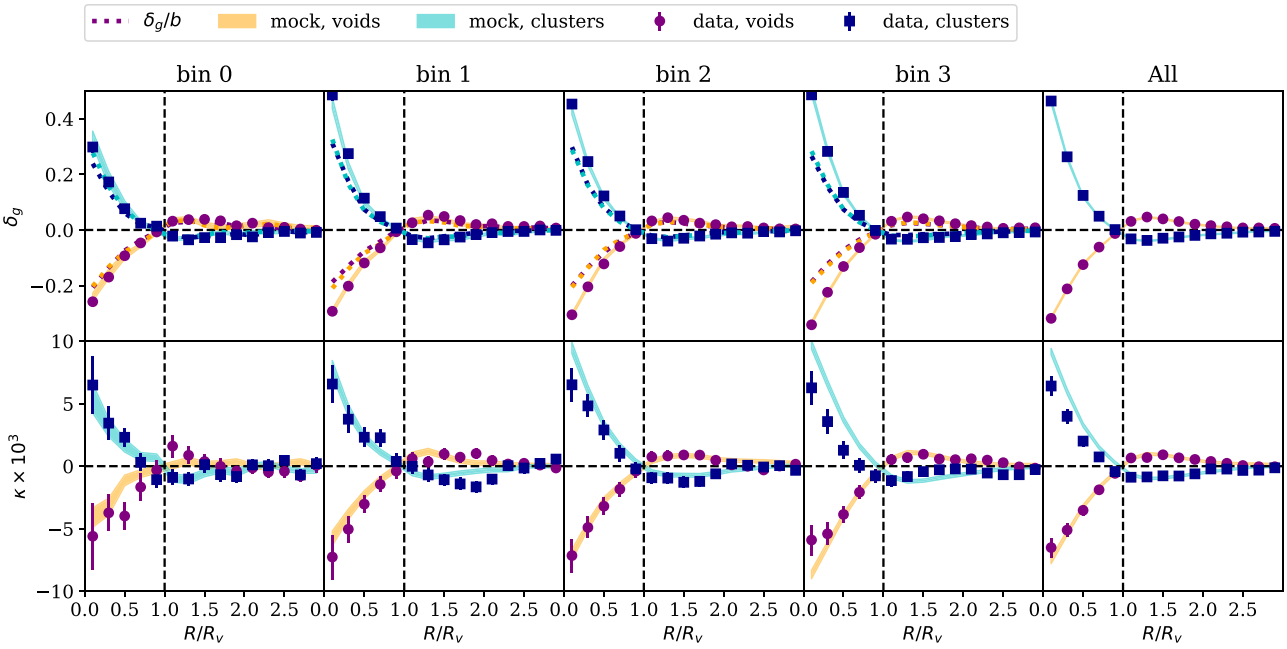

Figure 7. Upper panel: The averaged radial profile of stacked galaxy density in each redshift bin at the superstructure positions found in the mock (solid band) and data (points). The dotted lines show the mean profile divided by the linear galaxy bias measured in the mock and data, respectively. Lower panel: The averaged radial profile of stacked CMB lensing convergence. The lensing map has been smoothed by a Gaussian kernel of FWHM $= 1^\circ$ to suppress the small-scale power for the purpose of map rotation at the pixel level. The error bars come from Jackknife sampling of the superstructures in each redshift bin.

The lower panel of Fig. 7 shows the stacked radial profile of the κ-map. Similar to the case of the stacked galaxy density profile, the change of sign with a peak at $R \approx 1.3R_v$ is also present in the stacked κ profiles. For voids, the real and mock data sets show good consistency in general. For clusters, however, the simulation overpredicts the lensing signal in bin 3 significantly for $R < R_v$. Combining clusters in all four redshift bins, we find that the simulation also shows a 30 per cent excess compared to data, because the sample is dominated by the highest redshift bin. Due to the slightly more extended R_v distribution in the real data compared to the mock, especially in the highest redshift bin (see Fig. 6), we check whether or not including a weight, based on the ratio of the two R_v distributions, can reduce the difference between the data and the mock. However, the inclusion of this weight does not change the signal significantly.

We characterize the consistency between simulation result and data using the lensing amplitude A_κ, where $A_\kappa = \kappa_{\rm data}/\kappa_{\rm th}$. Assuming Gaussian likelihoods with $\mathcal{L} \propto \exp(-\chi^2/2)$ and using the Jackknife covariance for the combined case, we find $A_\kappa = 0.937 \pm 0.087$ for all voids and $A_\kappa = 0.712 \pm 0.076$ for all clusters. Assuming independence, this difference is formally 1.9σ, so hardly compelling evidence of an inconsistency; the combined result gives $A_\kappa = 0.811 \pm 0.057$.

In H21, the measured angular cross-correlation between CMB lensing and galaxy overdensity also has a lower amplitude, $A_\kappa = 0.901 \pm 0.026$, given the best-fitting *Planck* 2018 cosmological parameters, $\sigma_8 = 0.811$ and $\Omega_{\rm m} = 0.315$. We further measure the angular cross-correlation $C_\ell^{g\kappa}$ of the mock and compare it with data. In order to account for the difference in galaxy bias, we include galaxy autocorrelation C_ℓ^{gg} and compare the bias-independent quantity $R = C_\ell^{g\kappa}/(C_\ell^{gg})^{-1/2}$. The lensing amplitude A_κ is then given by $A_\kappa = R^{\rm data}/R^{\rm mock}$. We compare the binned modes with $10 \leq \ell < 500$, assuming a diagonal covariance where the diagonal terms, following equations (12) and (13) in H21. We obtain the following values for A_κ in the four bins: 0.84 ± 0.06, 0.81 ± 0.05, 0.86 ± 0.04, and 0.79 ± 0.04, and for the unbinned case, $A_\kappa = 0.85 \pm 0.03$, consistent with the stacked result. This may suggest that the lower lensing signal is likely contributed by high-density peaks.

In summary, the selection of superstructures based on the projected galaxy number density seems to pick up genuine superstructures. This is evident from the perfect agreement of galaxy number density profiles between our mocks and the observed data, and the reasonable agreement between the predicted CMB lensing convergence profiles and the observed versions. The latter suggests that the spatial variation of gravitational potentials is genuinely correlated with the superstructures. This gives us confidence in using them to study their expected temporal variations, which should be found via their ISW imprints on the CMB temperature maps. We therefore keep our catalogues fixed and 'unblind' our analysis from this stage.

5.2 Stacked ISW map

We remove $\ell < 10$ modes from the *Planck* 2018 CMB temperature map and the simulated ISW map to reduce the effect of the imperfectly simulated large-scale modes in the simulated ISW map as shown in Fig. 3. A comparison of the stacked ISW profiles in data and simulation is presented in Fig. 8. The quasi-linear theory prediction from the lensing potential gives consistent results, as does the full non-linear calculation, shown in the thin and broad solid lines, respectively. Given the size of the error, the data show general consistency with the simulation. In the void case, it is noticeable that in bin 0, the measurement from data is slightly positive, whereas in bin 1, the data have a larger amplitude compared to the mock with $R < R_v$. The level of fluctuations in the four measurements suggests that these deviations are not statistically significant. We use the covariance matrix obtained from 1000 sets of random void positions to quantify the consistency between data and simulation. Given 15 degrees of freedom (DOF), the χ^2 for each redshift bin is 8.9, 11.1, 16.2, and 11.8. The null test of the data signal gives

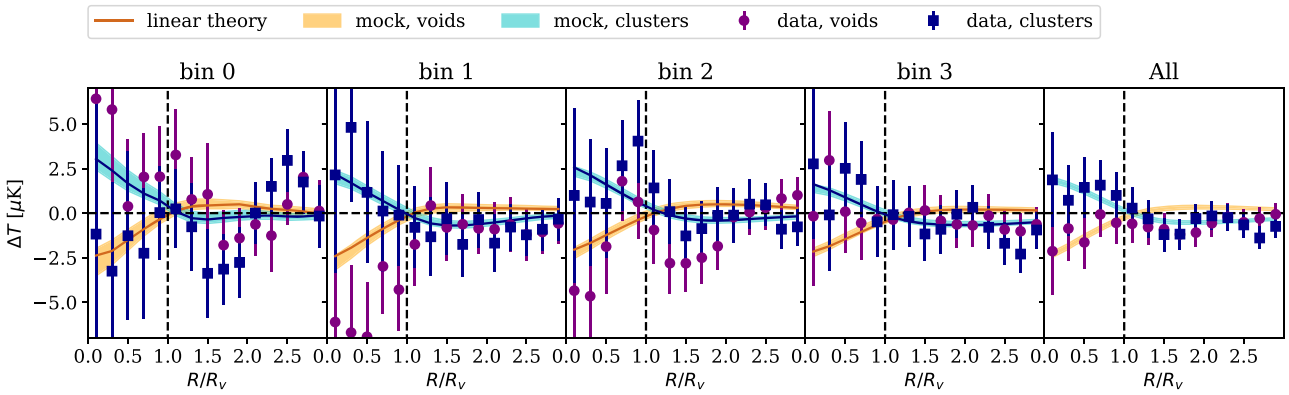

Figure 8. The averaged radial profile of stacked ISW temperature in each redshift bin at the superstructure positions found in the mock (solid band) and data (points). The quasi-linear predictions are shown by the thin lines. The *Planck* 2018 CMB temperature map is used for data with $\ell < 10$ modes removed. The error bars come from Jackknife sampling of the superstructures in each redshift bin.

χ^2 of 8.1, 12.7, 15.2, and 10.2. In general, the data do not show a preference for the simulation prediction over a null signal. For clusters, similar level of statistical fluctuations is present, with $\chi^2 =$ 11.3, 7.6, 10.8, and 16.1 for data compared to simulation, and $\chi^2 =$ 10.5, 8.9, 11.3, and 17.3 for the null test. Combining voids in all four bins, we find that $\chi^2 = 12.6$ for simulation and $\chi^2 = 10.1$ for a null signal. The larger χ^2 for the simulation is probably due to the slightly negative signal at $R > R_v$. The combined cluster result shows $\chi^2 =$ 11.1 for simulation and $\chi^2 = 15.1$ for null signal. We characterize the consistency between simulation result and data using the ISW amplitude $A_{\rm ISW}$, where $A_{\rm ISW} = \Delta T_{\rm data}/\Delta T_{\rm th}$. Assuming Gaussian likelihoods with $\mathcal{L} \propto \exp(-\chi^2/2)$, we find $A_{\rm ISW} = -0.10 \pm 0.69$ for all voids and $A_{\rm ISW} = 1.52 \pm 0.72$ for all clusters. The combined result gives $A_{\rm ISW} = 0.68 \pm 0.50$. Therefore, given the size of error, the measurements are fully consistent with the ΛCDM prediction; however, there is also no clear detection of this signal.

5.3 Comparison with K19

We investigate the possible causes of the excess signal in K19. We attempt to apply the same void finding algorithm as K19 but with a few differences. First, they used redshift bins with a comoving width of $100\,h^{-1}$ Mpc between $0.2 < z < 0.9$, whereas our bins are much wider in our fiducial setting. Secondly, due to the larger galaxy bias of the redMaGiC sample, they use a fixed $\delta_* = -0.3$ in the void finding algorithm across all redshift bins and a comoving smoothing scale of $50\,h^{-1}$ Mpc. In our fiducial setting, we have chosen to define δ_* to correspond to the lowest 10 per cent in density and applied a comoving smoothing scale of $20\,h^{-1}$ Mpc. Thirdly, in K19 a subsample of supervoids, with $R_v > 100\,h^{-1}$ Mpc in particular, gave the excess signal, whereas in our fiducial void sample, we have not made selections based on void properties. Finally, the void sample in K19 is only within the DES footprint, whereas our sample covers a larger region.

To begin with, we make the assumption that differences in the void finding process would not lead to an inconsistent stacking signal, because the underlying structures found should correspond to the same physical underdensities. In this case, one possibility could be that the excess is only contributed by the supervoids with $R_v > 100\,h^{-1}$ Mpc.

Thus, we look at such subsample with our fiducial setting. This gives a total of 151 simulated voids and 187 voids in the actual data. This number is smaller than one would expect from the K19 sample, which comprises 87 voids with $R_v > 100\,h^{-1}$ Mpc within the DES footprint, if it were extended about 3 times to the same size as the Legacy Survey. This difference can be attributed to the thicker redshift slices used in our analysis. An additional factor is that most of the DES Y1 region is masked owing to our completeness cut; thus, we may also lose a number of voids from that area. The stacked ISW profiles are shown on the right-hand panel of Fig. 9. The overall signal from data (purple dots) shows good consistency with our simulation results (yellow band). On the same plot, we also copy the results from K19. While their theoretical prediction (grey solid line) seems to be smaller than ours, their void signal from the DES sample (blue band) is much stronger. The difference in the theoretical prediction is plausibly due to the difference involved in the void-finding procedure. Using the covariance matrix from 1000 sets of random void samples, the χ^2 is 16.3 compared to simulation and 16.5 compared to a null signal with DOF = 15. This suggests that in our fiducial sample, the large voids with $R_v > 100\,h^{-1}$ Mpc do not cause an excess ISW signal.

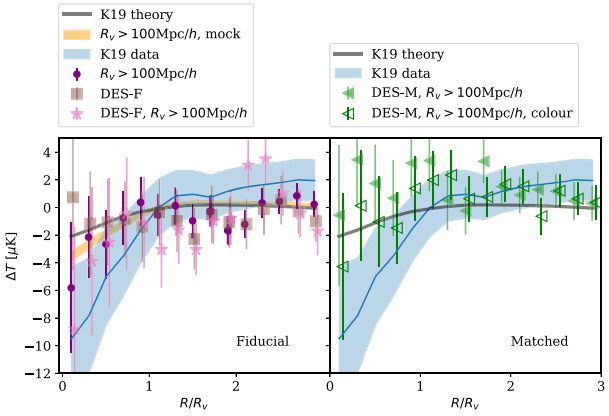

Figure 9. Stacked void profiles for a few subsamples chosen to match the K19 measurements (data shown as a blue band and theory shown as a grey solid line). The subsamples involving our fiducial setting are shown on the left-hand panel, including: selection of void radius $R_v > 100\,h^{-1}$ Mpc (purple circle); selection within the DES footprint (brown square); and selection within DES footprint as well as cut on R_v (pink star). We also consider subsamples that are more closely matched to K19 in the void-finding process within the DES footprint with and without a redMaGiC-like colour selection (shown on the right-hand panel as open and filled green triangles). The error bars are given by Jackknife resampling.

Another possibility is that the K19 excess is due to cosmic variance. To test this, we apply the same survey mask from the DES footprint, giving a subsample of 173 voids, with 40 voids among them having $R_v > 100\,h^{-1}$ Mpc. As shown on the right-hand panel of Fig. 9, the stacked signal using all voids within the DES footprint (brown squares) is consistent with zero, but selecting the large voids (pink stars) does result in a mean signal closer to that measured in K19. However, given the size of the error bars, the overall signal is consistent with both a null signal and the simulation prediction.

The above investigation suggests that the excess signal may be due to differences in the redshift binning and parameter choices in the void-finding process. Thus, we try to follow the procedure outlined in K19 (and references therein) as closely as possible in order to see if we can reproduce their signal. We split our photometric sample in the redshift range $0.2 < z < 0.8$ into bins of comoving width of $100\,h^{-1}$ Mpc. We exclude bins beyond $z \approx 0.7$ due to a sharp drop in number density. This gives a total of 11 redshift bins. We also create another sample that has a matched colour distribution in $g - W_1$ versus $r - z$ and $g - r$ versus $r - z$ as the DESY1A1 RedMaGiC sample. The details of the selection criteria can be found in Appendix A. Such a selection removes roughly half of the sample compared to the unmatched one. To account for the masked DES Y1 region, we relax the completeness threshold for the mask to 30 per cent so that most of the DES Y1 region is now included. The completeness weighting and stellar density correction is then applied to each density map in a similar way to H21. Finally, due to the large photo-z tail, we expect neighbouring bins to overlap significantly. In K19, a careful pruning of voids was applied by shifting the redshift binning by a small amount. In this case, we apply a simplified version, where for neighbouring bins we remove the voids in the higher redshift bin if their centre lies within $0.5R_v$ of the voids in the lower redshift bin. We check that this removes most of the overlapping voids. We also apply the same smoothing scale as in K19, $\sigma = 50\,h^{-1}$ Mpc, in void finding. We find 75 and 64 voids with $R_v > 100\,h^{-1}$ Mpc inside the DES footprint with and without colour space constraints, respectively, comparable to the 87 samples in K19. The stacked signal from these 'matched' samples is shown on the left-hand panel of Fig. 9 as green open triangles (with colour selection) and filled triangles (without colour selection). These signals are slightly positive at $R < R_v$ and do not reproduce the excess signal shown in K19 (blue band). Thus, the excess signal may be due to other details in the void catalogue construction. For example, the small redshift bins can be affected by the uncertainty of our photo-z sample, which has a median of $|\Delta z| = 0.027$ but with a large non-Gaussian tail.

To summarize, we have attempted to compare the ISW signal from our void sample with K19 by investigating cuts on the void size, cosmic variance, and void-finding procedure. In the first two cases, we do not see a clear deviation from our simulation prediction based on the ΛCDM cosmology. In the last case, we obtain a signal that is consistent with ΛCDM, rather than roughly three times larger than the theoretical prediction from K19. This difference may be caused by details in the galaxy catalogue such as the galaxy sample and the photometric redshifts.

5.4 Searching for higher ISW signal

In this section, we look at the dependence of the signal to noise of the stacked ISW profile on supercluster properties. The purpose here is to see whether the excess ISW can be reproduced in by applying specific selections, rather than trying to claim a higher significance detection. Specifically, we focus on R_v and δ_c, and in each case, we split the sample into the most extreme 10 per cent and 50 per cent and compare the signal-to-noise with the full sample. We use the simulation to determine the mean expected signal (thus the signal itself is noise free) and we show realistic errors by computing the covariance from 1000 sets of random void positions within the DESI Legacy Survey footprint and stack using the *Planck* CMB map. As shown in the upper panel in Fig. 10, selecting the 10 per cent most extreme objects in terms of R_v or δ_c can boost the predicted ISW signal by about a factor of 2. From the lower panel in Fig. 10, it is clear that the larger R_v has a smaller uncertainty compared to the more extreme δ_c selections with the same number of objects. This may be due to the fact that with the larger R_v selection, the stacked profile is effectively averaging over a larger scale on the CMB map, thus reducing the noise on the profile.

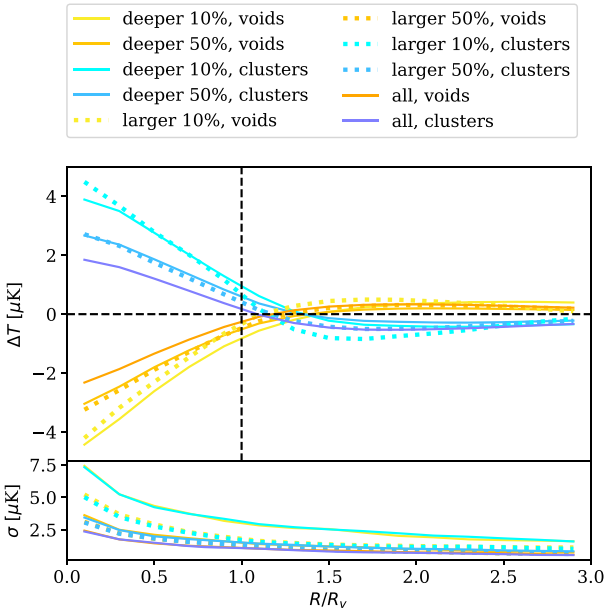

Figure 10. Stacked ISW profile split by central depth δ_c (solid line) and size R_v (dotted line) using superstructures in the mock catalogue. The split is using the most extreme 10 per cent, 50 per cent, and the full sample in each case. Error bars are given by 1000 sets of random void stacking using the *Planck* CMB map.

We measure the constraints on $A_{\rm ISW}$ for these selections in data. Focusing on the 10 per cent and 50 per cent of the superstructures with the largest R_v, we find that the data measurements show an increased signal especially in density peaks, with $A_{\rm ISW} = 0.10 \pm 0.99$, 0.57 ± 0.71 for voids and $A_{\rm ISW} = 1.47 \pm 0.77$, 2.59 ± 0.73 for clusters. Limiting the sample to the 10 per cent and 50 per cent with the most extreme δ_c, we find that the data do not show a significant boost in the ISW signal, and $A_{\rm ISW} = 0.15 \pm 1.24$, 0.32 ± 0.89 for voids and $A_{\rm ISW} = 0.83 \pm 1.26$, 0.25 ± 0.89 for clusters. Combining the voids and clusters in the δ_c selection, one finds $A_{\rm ISW} = 0.75 \pm 0.83$, 0.58 ± 0.59 for the 10 per cent and 50 per cent of the total sample, which does not improve the significance of the signal compared to the full sample. On the other hand, in the R_v case combining voids and clusters, $A_{\rm ISW} = 0.96 \pm 0.61$, 1.55 ± 0.51. The constraints on R_v from the higher R_v subsamples and the full sample are statistically consistent with 0.3σ and 1.2σ for the 10 per cent and 50 per cent cases, respectively. Therefore, by constraining on a larger R_v sample, it is statistically possible to obtain a larger mean ISW signal, leading to a more significant detection of the ISW amplitude,

$A_{\rm ISW}$. However, we emphasize that this selection is a posteriori, and one should take these results with caution.

6 CONCLUSIONS

In this work, we have constructed a catalogue of superstructures, using tomographic data with $0 < z < 0.8$ in the DESI Legacy Imaging Survey. We adopt the void-finding algorithm described in Sánchez et al. (2017), taking the lowest 10 per cent and highest 5 per cent pixels of the galaxy density field after 2D Gaussian smoothing with $\sigma = 20\,h^{-1}$ Mpc. The aim has been to test the excess ISW signal from supervoids claimed in literature (Granett et al. 2008; Kovács et al. 2019). To compare our results with the ΛCDM model prediction, we constructed a mock catalogue using the *Multidark* simulation. The galaxy number density and linear and non-linear galaxy biases are matched to those found in our previous work on the DESI Legacy Imaging Survey (Hang et al. 2021: H21), and we applied a redshift error to match the photo-z precision found in H21. The properties of the superstructures and the stacked galaxy density profiles around these superstructures are consistent between the mock and the data. We also created the corresponding lensing convergence and ISW maps.

Subsequently, we looked at the stacked CMB lensing convergence and CMB temperature using the *Planck* 2018 maps at the centre of these superstructures, scaled by the void/cluster radius R_v. The comparison between the stacked lensing signal agrees well in the void case, but the cluster signal seems to be slightly overpredicted in the highest redshift bin. Using the covariance matrix from 1000 sets of randomized superstructure positions, we quantify the consistency between simulation and data via the lensing amplitude A_κ and find $A_\kappa = 0.81 \pm 0.06$ from combining the voids and clusters. This is largely driven by the highest redshift bin, which contains the most clusters. In H21, we favoured a lensing amplitude of $A_\kappa = 0.93 \pm 0.03$ compared to the theoretical prediction from the *Planck* 2018 best-fitting cosmology, using cross-correlation in spherical harmonic space (therefore essentially utilizing all pixels, rather than density peaks and troughs). The amplitude of the CMB lensing signal is consistent with our result from superstructures, although we note that the voids and clusters are in $1.9\,\sigma$ tension, with $A_\kappa = 0.937 \pm 0.087$ for all voids and $A_\kappa = 0.712 \pm 0.076$ for all clusters. Despite this, the level of disagreement between our mocks and data for the lensing signal is negligibly small for the purpose of the ISW study, as its measurement is much noisier.

The stacked ISW signals are in general consistent with the simulation results – but also with a null signal, reflecting the low signal to noise of the ISW effect. Specifically, we do not detect a significant signal from the void catalogue and only a marginal signal from clusters. Combining the superstructures, we find the ISW amplitude to be $A_{\rm ISW} = 0.68 \pm 0.50$, somewhat weaker than the cross-correlation result from H21, which gave $A_{\rm ISW} = 1.10 \pm 0.31$ (although both measurements are consistent). Therefore, we do not claim a detected ISW signal using this sample.

We compare our results with K19, Kovács et al. (2019), who reported a 3σ excess ISW signal compared to the ΛCDM prediction from supervoids with void radius $R_v > 100\,h^{-1}$ Mpc, using the DES redMaGiC sample within a similar redshift range to ours. Using our fiducial settings described above, we do not find any excess signal from voids with the same size cut, or within the same survey mask. Two subsamples are then constructed to match the redshift binning and void-finding procedure in K19 as closely as possible within the DES footprint, with and without a redMaGiC-like colour selection. The stacked ISW profiles from the voids found in these samples also do not show any anomalous signal.

Lastly, we look at the dependence of the ISW signal on the void properties and discuss whether this can be used to explain a higher detection of the ISW signal from suitably chosen superstructures. We show that the mean ISW signal from the mock data set is amplified by excluding smaller or less extreme superstructures, while the shot noise increases. Applying the same selections to the data, we find no significant improvement in the constraint on the ISW amplitude $A_{\rm ISW}$ from more extreme superstructures, although there is a boost in $A_{\rm ISW}$ from density peaks with larger R_v. The most extreme subset conditioning on the 10 per cent largest R_v gives $A_{\rm ISW} = 0.96 \pm 0.61$, and the 95 per cent upper limit is 2.16. However, we emphasize that the selection of this subset is not a priori. The increase in the mean signal is therefore inevitably overestimated due the look-elsewhere effect.

In summary, then, our results from investigating the impact of superstructures on the CMB do not reveal any compelling discrepancy with ΛCDM. The CMB lensing results for superstructures independently favour an approximately 10 per cent reduction in amplitude relative to the *Planck* 2018 prediction in very close agreement with our conclusion from the overall galaxy-lensing cross-correlation in H21, which we argued favoured a matter density at the low end of the range permitted by *Planck*. The evidence for this reduced lensing amplitude is present in both voids and clusters although the latter favour a stronger signal at the 1.9σ level; it will be interesting to see if this tension becomes more significant in future data sets. Similarly, the ISW signal from stacked superstructures is consistent with the H21 cross-correlation result and not in significant disagreement with ΛCDM. Formally, the 95 per cent confidence upper limit on $A_{\rm ISW}$ from superstructures is 1.51, and therefore we do not reproduce literature claims of anomalous superstructure ISW signals at several times the ΛCDM prediction. We have tried to vary our analysis in order to mimic more closely the selection involved in these claims but have not succeeded in raising the ISW signal. Presumably some small differences in method remain. But the important point is that any such excess is apparently not robust, since we were not able to produce an excess signal even by exploring a number of alternative forms of superstructure selection.

A similar investigation has been performed by Dong et al. (2021), who measured the cross-correlation between the 'low-density position' (LDP) and the CMB using the DESI Legacy Survey. In this work, they detected the ISW effect from their underdense regions with a significance of 3.4σ, and this signal is fully consistent with the ΛCDM prediction.

ACKNOWLEDGEMENTS

QH was supported by the Edinburgh Global Research Scholarship and the Higgs Scholarship from Edinburgh University. SA and JAP were supported by the European Research Council under grant number 670193 (the COSFORM project). YC acknowledges the support of the Royal Society through the award of a University Research Fellowship and an Enhancement Award.

The Legacy Surveys consist of three individual and complementary projects: the Dark Energy Camera Legacy Survey (DECaLS; NOAO Proposal ID # 2014B-0404; PIs: David Schlegel and Arjun Dey), the Beijing–Arizona Sky Survey (BASS; NOAO Proposal ID # 2015A-0801; PIs: Zhou Xu and Xiaohui Fan), and the Mayall z-band Legacy Survey (MzLS; NOAO Proposal ID # 2016A-0453; PI: Arjun Dey). DECaLS, BASS, and MzLS together include data obtained, respectively, at the Blanco telescope, Cerro Tololo Inter-American

Observatory, National Optical Astronomy Observatory (NOAO); the Bok telescope, Steward Observatory, University of Arizona; and the Mayall telescope, Kitt Peak National Observatory, NOAO. The Legacy Surveys project is honoured to be permitted to conduct astronomical research on Iolkam Du'ag (Kitt Peak), a mountain with particular significance to the Tohono O'odham Nation.

NOAO is operated by the Association of Universities for Research in Astronomy (AURA) under a cooperative agreement with the National Science Foundation.

This project used data obtained with the Dark Energy Camera (DECam), which was constructed by the Dark Energy Survey (DES) collaboration. Funding for the DES Projects has been provided by the U.S. Department of Energy, the U.S. National Science Foundation, the Ministry of Science and Education of Spain, the Science and Technology Facilities Council of the United Kingdom, the Higher Education Funding Council for England, the National Center for Supercomputing Applications at the University of Illinois at Urbana-Champaign, the Kavli Institute of Cosmological Physics at the University of Chicago, Center for Cosmology and Astro-Particle Physics at the Ohio State University, the Mitchell Institute for Fundamental Physics and Astronomy at Texas A&M University, Financiadora de Estudos e Projetos, Fundacao Carlos Chagas Filho de Amparo, Financiadora de Estudos e Projetos, Fundacao Carlos Chagas Filho de Amparo a Pesquisa do Estado do Rio de Janeiro, Conselho Nacional de Desenvolvimento Cientifico e Tecnologico and the Ministerio da Ciencia, Tecnologia e Inovacao, the Deutsche Forschungsgemeinschaft, and the Collaborating Institutions in the Dark Energy Survey. The Collaborating Institutions are Argonne National Laboratory, the University of California at Santa Cruz, the University of Cambridge, Centro de Investigaciones Energeticas, Medioambientales y Tecnologicas-Madrid, the University of Chicago, University College London, the DES-Brazil Consortium, the University of Edinburgh, the Eidgenossische Technische Hochschule (ETH) Zurich, Fermi National Accelerator Laboratory, the University of Illinois at Urbana-Champaign, the Institut de Ciencies de l'Espai (IEEC/CSIC), the Institut de Fisica d'Altes Energies, Lawrence Berkeley National Laboratory, the Ludwig-Maximilians Universitat Munchen and the associated Excellence Cluster Universe, the University of Michigan, the National Optical Astronomy Observatory, the University of Nottingham, the Ohio State University, the University of Pennsylvania, the University of Portsmouth, SLAC National Accelerator Laboratory, Stanford University, the University of Sussex, and Texas A&M University.

BASS is a key project of the Telescope Access Program (TAP), which has been funded by the National Astronomical Observatories of China, the Chinese Academy of Sciences (the Strategic Priority Research Program 'The Emergence of Cosmological Structures' grant # XDB09000000), and the Special Fund for Astronomy from the Ministry of Finance. The BASS is also supported by the External Cooperation Program of Chinese Academy of Sciences (grant # 114A11KYSB20160057), and Chinese National Natural Science Foundation (grant # 11433005).

The Legacy Survey team makes use of data products from the Near-Earth Object Wide-field Infrared Survey Explorer (NEOWISE), which is a project of the Jet Propulsion Laboratory/California Institute of Technology. NEOWISE is funded by the National Aeronautics and Space Administration.

The Legacy Surveys imaging of the DESI footprint is supported by the Director, Office of Science, Office of High Energy Physics of the U.S. Department of Energy under contract no. DE-AC02-05CH11231, by the National Energy Research Scientific Computing Center, a DOE Office of Science User Facility under the same contract, and by the U.S. National Science Foundation, Division of Astronomical Sciences under contract no. AST-0950945 to NOAO.

The CosmoSim data base used in this paper are a service by the Leibniz-Institute for Astrophysics Potsdam (AIP). The MultiDark data base was developed in cooperation with the Spanish MultiDark Consolider Project CSD2009-00064.

The authors gratefully acknowledge the Gauss Centre for Supercomputing e.V. (www.gauss-centre.eu) and the Partnership for Advanced Supercomputing in Europe (PRACE, http://www.prace-ri.eu) for funding the MultiDark simulation project by providing computing time on the GCS Supercomputer SuperMUC at Leibniz Supercomputing Centre (LRZ, http://www.lrz.de).

DATA AVAILABILITY

All of the observational data sets used in this paper are available through the Legacy Survey website: http://legacysurvey.org/dr8/. The codes used in this analysis along with several processed data products can be accessed at: https://gitlab.com/qianjunhang/desi-legacy-survey-superstructure-stacking.

REFERENCES

Ahumada R. et al., 2020, ApJS, 249, 3
Alam S. et al., 2015, ApJS, 219, 12
Asgari M. et al., 2021, A&A, 645, A104
Beck R., Csabai I., Rácz G., Szapudi I., 2018, MNRAS, 479, 3582
Behroozi P. S., Wechsler R. H., Wu H.-Y., 2013, ApJ, 762, 109
Cabré A., Gaztañaga E., Manera M., Fosalba P., Castander F., 2006, MNRAS, 372, L23
Cai Y.-C., Cole S., Jenkins A., Frenk C. S., 2010, MNRAS, 407, 201
Cai Y.-C., Neyrinck M. C., Szapudi I., Cole S., Frenk C. S., 2014, ApJ, 786, 110
Cai Y.-C., Neyrinck M., Mao Q., Peacock J. A., Szapudi I., Berlind A. A., 2017, MNRAS, 466, 3364
Cawthon R. et al., 2018, MNRAS, 481, 2427
Clampitt J., Cai Y.-C., Li B., 2013, MNRAS, 431, 749
Darwish O. et al., 2021, MNRAS, 500, 2250
Dey A. et al., 2016, Proc. SPIE Conf. Ser. Vol. 9908, Ground-based and Airborne Instrumentation for Astronomy VI. SPIE, Bellingham, p. 99082C
Dey A. et al., 2019, AJ, 157, 168
Dong F., Yu Y., Zhang J., Yang X., Zhang P., 2021, MNRAS, 500, 3838
Doux C., Penna-Lima M., Vitenti S. D. P., Tréguer J., Aubourg E., Ganga K., 2018, MNRAS, 480, 5386
Flaugher B. et al., 2015, AJ, 150, 150
Fosalba P., Gaztañaga E., Castander F. J., 2003, ApJ, 597, L89
Giannantonio T., Scranton R., Crittenden R. G., Nichol R. C., Boughn S. P., Myers A. D., Richards G. T., 2008, Phys. Rev. D, 77, 123520
Giannantonio T. et al., 2016, MNRAS, 456, 3213
Górski K. M., Hivon E., Banday A. J., Wandelt B. D., Hansen F. K., Reinecke M., Bartelmann M., 2005, ApJ, 622, 759
Granett B. R., Neyrinck M. C., Szapudi I., 2008, ApJ, 683, L99
Hang Q., Alam S., Peacock J. A., Cai Y.-C., 2021, MNRAS, 501, 1481 (H21)
Hartlap J., Simon P., Schneider P., 2007, A&A, 464, 399
Ho S., Hirata C., Padmanabhan N., Seljak U., Bahcall N., 2008, Phys. Rev. D, 78, 043519
Hu W., 2000, Phys. Rev. D, 62, 043007
Ilbert O. et al., 2009, ApJ, 690, 1236
Joudaki S. et al., 2020, A&A, 638, L1
Klypin A., Yepes G., Gottlöber S., Prada F., Heß S., 2016, MNRAS, 457, 4340
Kovács A., 2018, MNRAS, 475, 1777
Kovács A. et al., 2017, MNRAS, 465, 4166
Kovács A. et al., 2019, MNRAS, 484, 5267 (K19)

Krolewski A., Ferraro S., Schlafly E. F., White M., 2020, J. Cosmology Astropart. Phys., 2020, 047
Lewis A., Challinor A., 2006, Phys. Rep., 429, 1
Liske J. et al., 2015, MNRAS, 452, 2087
Nadathur S., Crittenden R., 2016, ApJ, 830, L19
Nadathur S., Hotchkiss S., Sarkar S., 2012, J. Cosmology Astropart. Phys., 2012, 042
Newman J. A. et al., 2013, ApJS, 208, 5
Neyrinck M. C., 2008, MNRAS, 386, 2101
Okamoto T., Hu W., 2003, Phys. Rev. D, 67, 083002
Peacock J. A., Bilicki M., 2018, MNRAS, 481, 1133
Planck Collaboration I, 2018a, A&A, 641, A1
Planck Collaboration VI, 2018b, A&A, 641, A6
Planck Collaboration VIII, 2018c, A&A, 641, A8
Pollina G., Hamaus N., Dolag K., Weller J., Baldi M., Moscardini L., 2017, MNRAS, 469, 787
Prada F., Klypin A. A., Cuesta A. J., Betancort-Rijo J. E., Primack J., 2012, MNRAS, 423, 3018
Rees M. J., Sciama D. W., 1968, Nature, 217, 511
Riebe K. et al., 2013, Astron. Nachr., 334, 691
Sachs R. K., Wolfe A. M., 1967, ApJ, 147, 73
Sánchez C. et al., 2017, MNRAS, 465, 746
Scodeggio M. et al., 2018, A&A, 609, A84
Scranton R. et al., 2003, preprint (astro-ph/0307335)
Seljak U., 1996, ApJ, 460, 549
Singh S., Mandelbaum R., Brownstein J. R., 2017, MNRAS, 464, 2120
Singh S., Mandelbaum R., Seljak U., Rodríguez-Torres S., Slosar A., 2020, MNRAS, 491, 51
Stölzner B., Cuoco A., Lesgourgues J., Bilicki M., 2018, Phys. Rev. D, 97, 063506
The Dark Energy Survey Collaboration, 2005, preprint (astro-ph/0510346)
Vielzeuf P. et al., 2021, MNRAS, 500, 464
Williams G. G., Olszewski E., Lesser M. P., Burge J. H., 2004, in Moorwood A. F. M., Iye M., eds, Proc. SPIE Conf. Ser. Vol. 5492, Ground-based Instrumentation for Astronomy. SPIE, Washington, USA, p. 787
Wright E. et al., 2010, AJ, 140, 1868
Zhou R. et al., 2020, MNRAS, 501, 3309

APPENDIX A: MATCHING REDMAGIC COLOUR SELECTION

In order to match the DESY1A1 redMaGiC galaxies as closely as possible, we compare their distribution in colour–colour space with a subsample of DECaLS galaxies in the same region (Fig. A1). We apply cuts in the $g - r$ versus $r - z$ plane based on the ratio of the normalized distribution. We exclude regions in this space where the ratio is smaller than a threshold set to 0.5. Such an exclusion does not affect the redMaGiC sample (about 92 per cent of our objects remain), but it results in a cut in low-redshift DECALS galaxies. The selected DECALS sample contains 1.8 million galaxies, about 3 times the redMaGiC sample. Fig. A2 shows the selected region in the colour–colour plane for our full sample used in Section 5.3 in the redshift range $0.2 < z < 0.8$ in the north and south parts of the DESI Legacy Survey.

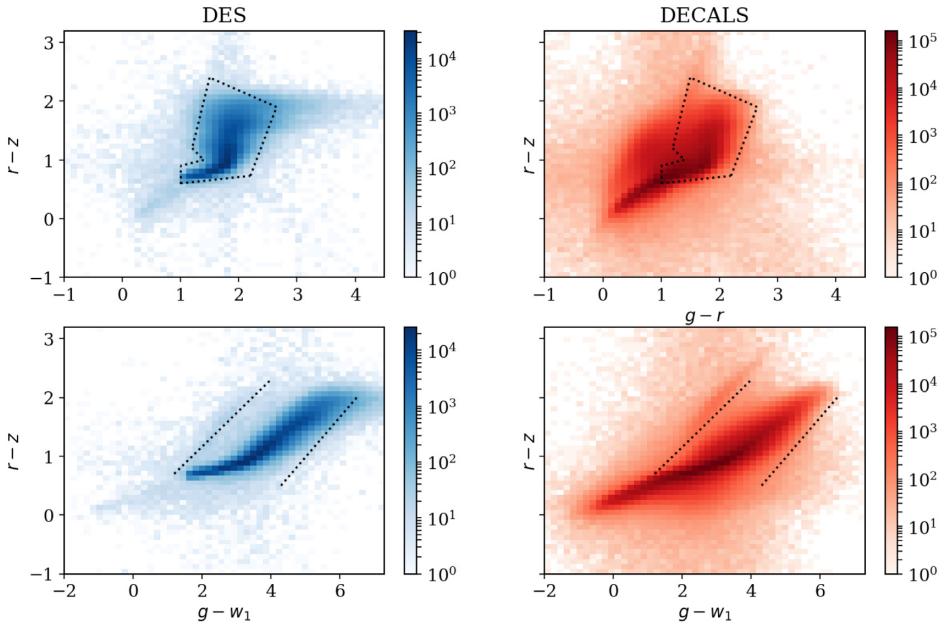

Figure A1. The comparison of redMaGiC (left, blue) and DECALS (right, red) samples in the same sky area in $g - r$ and $r - z$ plane (upper panel) and in $g - w_1$ and $r - z$ plane (lower panel). DECALS contains a large number of bluer objects compared to redMaGiC. The thin strip on the left side of the main sequence is likely to be residual stars. The black dotted box is the region used to take ratios.

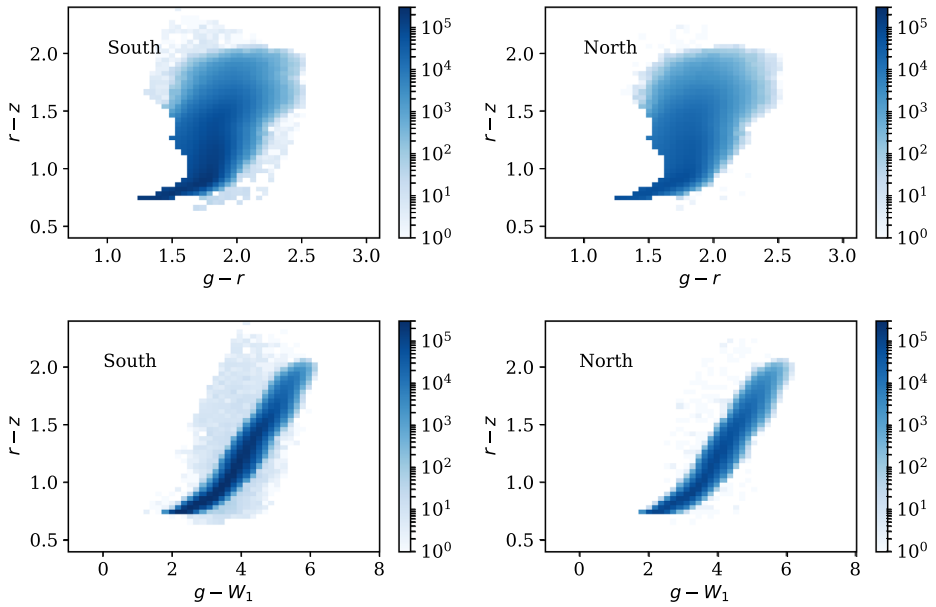

Figure A2. The selection in $g - r$ versus $r - z$ and $g - W_1$ versus $r - z$ colour space for the DESI Legacy Survey galaxy sample in the north and south regions, respectively, to match the DESY1A1 redMaGiC sample.

This paper has been typeset from a TEX/LATEX file prepared by the author.